

Mesoscale fractures control the scale dependences of seismic velocity and fluid flow in subduction zones

Yuya Akamatsu^{1*}, Hanaya Okuda², Manami Kitamura³, Michiyo Sawai⁴

1. Research Institute for Marine Geodynamics, Japan Agency for Marine-Earth Science and Technology (JAMSTEC), Japan

2. Kochi Institute for Core Sample Research, Japan Agency for Marine-Earth Science and Technology (JAMSTEC), Japan

3. Research Institute of Geo-Resources and Environment, Geological Survey of Japan, National Institute of Advanced Industrial Science and Technology, Japan

4. Department of Earth Sciences, Chiba University, Japan

* Corresponding author: Yuya Akamatsu (akamatsuy@jamstec.go.jp)

This is a non-peer reviewed preprint submitted to JGR: Solid Earth.

Abstract

Natural geological systems contain porosity structures of various scales that play different roles in geophysical properties, fluid flow, and geodynamics. To understand seismic activity associated with high pore-fluid pressure and fluid migration in subduction zones, it is necessary to explore the scale dependence of geophysical properties such as seismic velocity and permeability. Here, we compare laboratory-measured ultrasonic velocity (1 MHz) measured on core samples from the Susaki area in the Shimanto accretionary complex, SW Japan, with sonic velocity (15 kHz) measured by borehole logging experiments. Results show that P-wave velocity decreases from the laboratory (~6 km/s) to the borehole scales (~5 km/s). This scale-variant effect can be explained by a differential effective medium model whereby mesoscale porosity that is undetectable at the ultrasonic wavelength is introduced into the matrix phase with microscale porosity. Assuming typical apertures for micro- and mesoscale fractures, we estimate that the effective permeability can increase to 10^{-12} – 10^{-11} m² with increasing in the mesoscale porosity and decreasing P-wave velocity down to 4–5 km/s. These results indicate that seismic velocity anomalies and related seismic activity are associated with the presence of mesoscale fractures in subduction zones.

Plain Language Summary

In subduction zones, seismic activity are likely linked with fluid flow. Since the presence of pore fluid significantly modulates the elastic properties of rocks, seismic velocity structures have been utilized to infer the fluid behavior. However, interpretations of the seismic velocity structures have relied on experimental data from hand-sized samples, while seismic exploration involves multi-scale geological features over several kilometers. To bridge this scale gap and quantitatively assess fluid migration behavior from seismic velocity structures, it is essential to understand the scale dependence of elastic wave velocities in relation to pore structures. This study compares laboratory ultrasonic velocities, which reflect millimeter-scale pore structures, with logging sonic velocities, which reflect meter-

40 scale pore structures, using core samples and logging data at an on-land accretionary com-
41 plex in Japan which was originated from a deep subduction zone. The results indicate
42 that sonic logging velocities are consistently lower than laboratory ultrasonic velocities,
43 suggesting the presence of mesoscale fractures that cannot be observed in hand-sized sam-
44 ples. The mososcale fractures enable fluids to flow easily by several orders of magnitude
45 compared to the microscale fractures in hand-sized samples and thus play a substantial
46 role in fluid flow and seismic activities in subduction zones.

47 Key Points

- 48 • P-wave velocity of sedimentary rocks from accretionary complex decreases from labo-
49 ratory ultrasonic to borehole sonic scales
- 50 • Presence of mesoscale fractures as well as microscale porosity is indicated by up-
51 scaled effective medium modeling
- 52 • Mesoscale fractures can lead to high permeability and facilitate rapid fluid drainage
53 in subduction zones

54 Keywords

55 seismic velocity; upscaling; permeability; Nankai Trough

56 1 Introduction

57 Seismic activity in subduction zones has been related to high-pore fluid pressure and the
58 properties of the fluid drainage system on the basis that fluids play a dominant role in
59 controlling the frictional and rheological properties of rock (Saffer & Tobin, 2011). As
60 pore fluid can also influence the elastic properties of rock (Mavko et al., 2020), seismic
61 velocity structures have been obtained by seismological surveys and borehole logging
62 in various subduction zones to understand the causes of seismic activity (e.g., Audet &
63 Schwartz, 2013; Eberhart-Phillips et al., 2017; Kamei et al., 2013; Saffer, 2003; Shiraishi
64 et al., 2019). These velocity structures have revealed low-velocity anomalies and episodic
65 changes in velocity along the plate boundaries, which are likely associated with the
66 presence of high pore-fluid pressure and transient fluid migration (Tonegawa et al., 2022;
67 Tsuji et al., 2014).

68 To link seismic velocity and the pore fluid state, laboratory measurements of elastic wave
69 velocity using rock samples from the Nankai subduction zone, including drillcore from
70 the seafloor and an ancient accretionary complex on land, have been conducted (Hama-
71 hashi et al., 2013; Hoffman & Tobin, 2004; Kitamura et al., 2021; Raimbourg et al., 2011).
72 These studies have revealed the role of microscopic pores and cracks in controlling elas-
73 tic wave velocity, which has been applied to interpretations of observed seismic velocity
74 structures (Kitajima & Saffer, 2012; Tsuji et al., 2014). However, there is a large gap in
75 the scales of observations among laboratory measurements, borehole logging, and seismic
76 surveys, primarily because of the different probing frequencies and hence different wave-
77 lengths for measurements at each scale. Laboratory measurements are typically carried
78 out at ultrasonic frequency (~MHz) with hand-sized samples, and the measured elastic

79 wave velocity reflects millimeter-scale structures, such as microcracks and pores. In con-
80 trast, borehole sonic logging and seismological surveys are performed typically at frequen-
81 cies of \sim kHz and \sim Hz, respectively, which correspond to wavelengths of meters to kilo-
82 meters. Given that natural geological systems are heterogeneous and contain defects of
83 different scales at each scale of observation, the observed sonic and seismic velocities at
84 relatively low frequencies should be affected not only by microscopic pore structures but
85 also by larger-scale defects, such as fractures and faults (Bailly et al., 2019; Matonti et al.,
86 2015). As the permeability of rocks depends strongly on the dimensions of conduits, such
87 large-scale defects can lead to more effective fluid drainage compared with microscopic
88 pores and cracks, and may be related to the episodic occurrence of slow slip and tremor
89 associated with rapid fluid migration along subduction plate interfaces (Ide, 2010; Muñoz-
90 Montecinos & Behr, 2023). It is therefore crucial to explore the scale dependence of elas-
91 tic wave velocity to quantitatively relate the seismic velocity structures to seismic activity
92 in subduction zones via pore fluid behavior.

93 This study aims to obtain porosity structures at two scales (micro- and mesoscales) in
94 a rock mass sourced from a deep subduction zone and estimate the contribution of pore
95 fluid to seismic velocity at each scale. We use core samples from the Cretaceous Shimanto
96 belt in the Susaki area, Kochi, SW Japan, which is originated from the depths of seismo-
97 genic zone in a subduction zone similar to the present-day Nankai Trough (Itaba et al.,
98 2014). We first measured the P-wave velocity of the core samples at the MHz frequency
99 and dense intervals to obtain spatial variations in microscopic porosity at a macroscopic
100 scale. We then compared our data with sonic logging velocities measured at the kHz fre-
101 quency in the borehole. Results show a decrease in the P-wave velocity at larger scales,
102 suggesting the presence of mesoscale fractures. Finally, we estimated the effective perme-
103 ability of the rock at each scale, and discuss the potential role of mesoscale fractures on
104 seismic velocity and fluid flow in subduction zones.

105 2 Geologic setting and borehole logging data

106 The Susaki area is located in the Cretaceous Shimanto belt in SW Japan, which consists
107 of an accretionary complex associated with a plate subduction similar to the modern
108 Nankai Trough (Figure 1). Drilling was conducted in this area by the Geological Survey
109 of Japan (GSJ) in 2009, and continuous cores of \sim 600 m in total length were recovered
110 (Itaba et al., 2014). The drillcores consist mainly of sandstones and mudstones with inter-
111 calations of tuff layers, as well as quartz and calcite veins. Visual descriptions of the core
112 samples revealed few major faults in the core, with *mélange*-like deformation being ob-
113 served throughout the entire core (Itaba et al., 2014). As the drilling site is located in the
114 area which can be geologically extended from the Yokonami *mélange* and Awa *mélange*
115 (Taira, 1988), the core is presumed to have undergone a similar subduction–exhumation
116 history to the two *mélanges*. According to the previous studies that utilized fluid inclu-
117 sion analysis and vitrinite reflectance geothermometry, the *mélanges* reached a depth
118 equivalent to \sim 200 $^{\circ}$ C (i.e., the seismogenic zone depths) during the late Cretaceous and
119 were then exhumed (Hashimoto et al., 2012; Sakaguchi, 1999). This history indicates that
120 the entire core section from the Susaki area underwent the same subduction–exhumation
121 history as these *mélanges*.

122 Geophysical logging measurements in the studied boreholes were conducted by GSJ, and

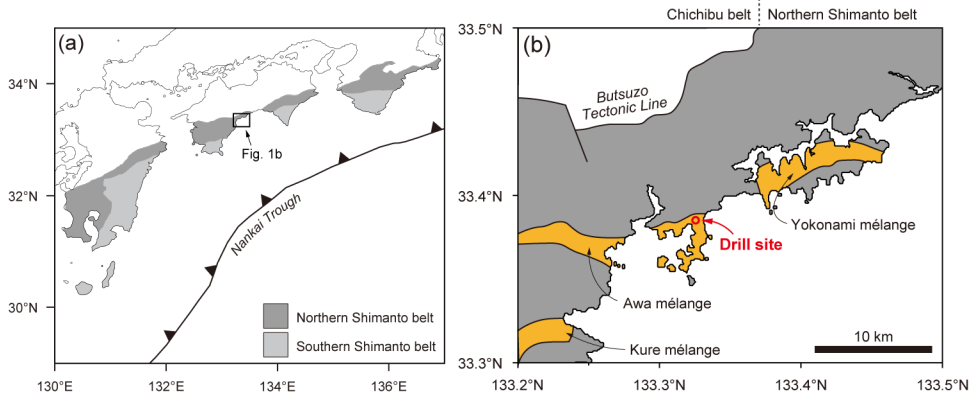


Figure 1 (a) Geological map of SW Japan; (b) map of the area around the site of the Susaki drillhole (modified after Hashimoto et al., 2012). Colored areas are mélanges zones.

123 downhole physical properties were obtained, including sonic velocity, electrical resistivity,
 124 and natural gamma rays (Itaba et al., 2014). Here, we focus on the sonic velocity data for
 125 comparison with ultrasonic velocity. Sonic logging was conducted at a probe frequency
 126 of ~ 15 kHz, which corresponds to a wavelength of ~ 0.3 m. This means that the downhole
 127 profile in sonic velocity reflects variations in submeter-scale structures. P-wave velocity
 128 from sonic logging was determined by picking the onset of the waveforms at each 10 cm
 129 increment in depth. During sonic logging, the hole was saturated with groundwater, so
 130 the measured velocities should be considered as values under water-saturated conditions.
 131 Although the sonic P-wave velocity shows an overall monotonic depth trend ranging from
 132 4 to 5.5 km/s (median of 5.0 km/s), sandstone layers tend to have slightly higher veloci-
 133 ties than mudstone layers (Figure 2).

134 3 Method

135 3.1 Measurement of ultrasonic velocity

136 To evaluate the spatial distribution of microscopic porosity in the Susaki core samples,
 137 we performed dense measurements of ultrasonic P-wave velocity under dry conditions at
 138 room temperature and pressure. Measurements were performed on whole core sections
 139 from the following intervals (Figure 2): 137–175 m (upper mudstone layer), 270–310 m
 140 (sandstone layer), and 420–470 m (lower mudstone layer). The core sections from these
 141 depths were reasonably intact and retained a cylindrical shape. P-wave velocity at the
 142 ultrasonic frequency was determined using a pulse transmission method, in which travel
 143 times of ultrasonic waves passing through the core were measured. The core sections were
 144 sandwiched by a pair of ultrasonic transducers with a resonant frequency of 1 MHz in the
 145 direction orthogonal to the core axis. An input pulse with an amplitude of 10 V was sent
 146 to the transducer by a pulse generator and was transmitted through the core, with the
 147 output signal being received by another transducer mounted on the opposite side and
 148 digitalized by an oscilloscope. The time of the first arrival of the ultrasonic wave was de-
 149 termined using the Akaike Information Criterion (Akamatsu et al., 2023; Sarout et al.,
 150 2009), and the P-wave velocity was then calculated by dividing the core diameter (56.5

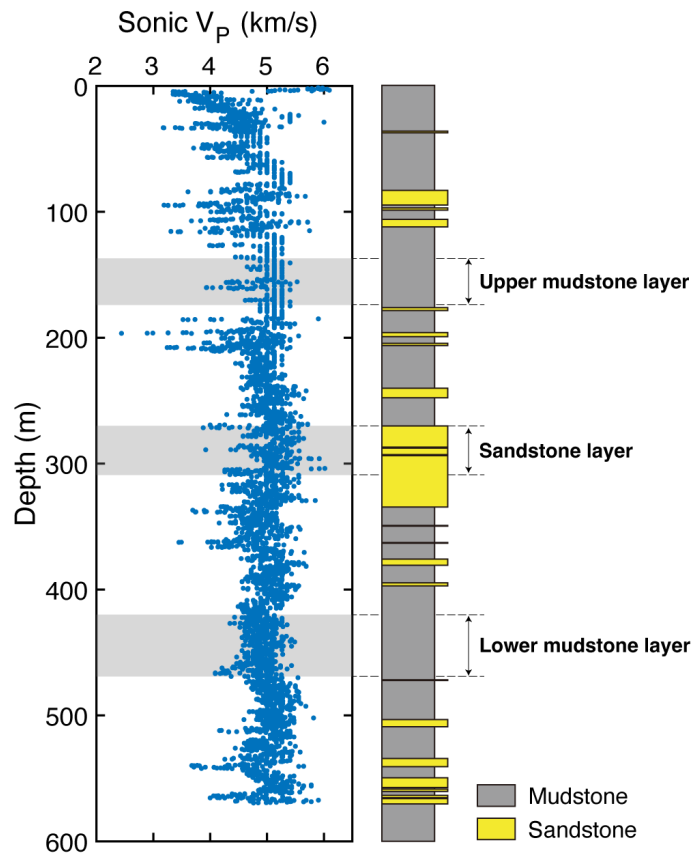


Figure 2 Downhole profile of P-wave velocity obtained by sonic logging in the Susaki boreholes and stratigraphic column of the core samples (modified after Itaba et al., 2014). Gray shading indicates the core intervals subjected to ultrasonic velocity measurements in this study.

151 mm for upper mudstone layer and 63.2 mm for sandstone and lower mudstone layers) by
 152 the travel time (Figure 3). This procedure was performed at each 5 cm interval for each
 153 core section over a total length of 128 m.

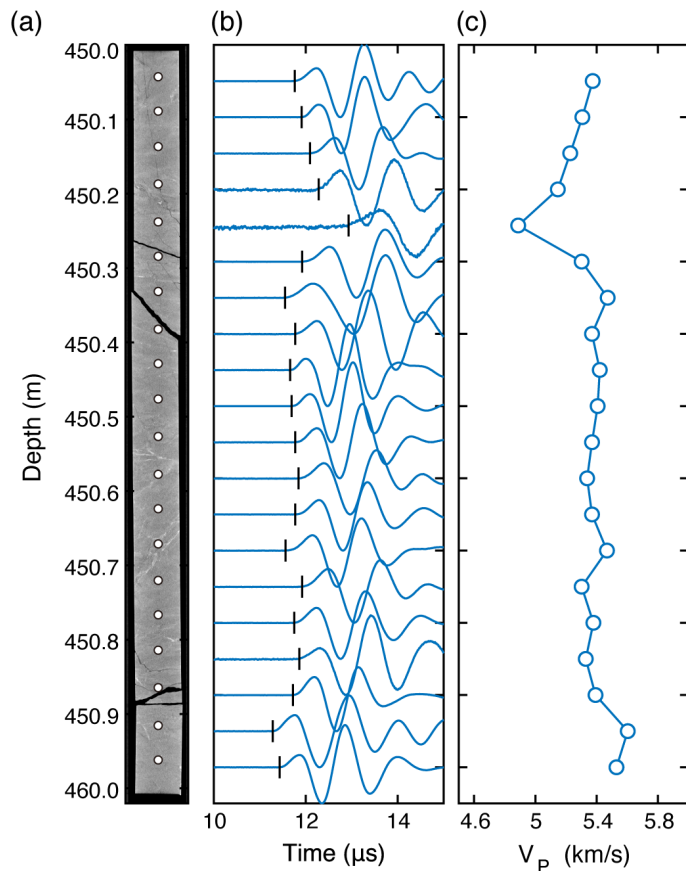


Figure 3 Example of results of ultrasonic velocity measurements. (a) Cross-section of a core sample (depths range 445–446 m) imaged using X-ray computed tomography. (b) Waveforms recorded at points indicated by white dots in (a). Vertical black lines denote the arrival times determined by the AIC. (c) Calculated P-wave velocities.

154 3.2 Effective medium modeling

155 Although the ultrasonic velocity measurements were performed under dry conditions,
 156 the borehole logging measurements from the Susaki boreholes were carried out under
 157 groundwater-saturated conditions. It is therefore necessary to correct the ultrasonic ve-
 158 locity for water-saturated (wet) conditions for accurate comparison with the sonic logging
 159 velocity. Effective medium theory allows us to predict the velocity under wet conditions
 160 from that under dry conditions if porosity and pore geometry are known. Here, we em-
 161 ployed the differential effective medium (DEM) model (Berryman et al., 2002; Mavko
 162 et al., 2020). For an isotropic medium containing randomly oriented spheroidal (penny-
 163 shaped) pores, the effective bulk modulus K^* and shear modulus G^* can be calculated as

164 follows:

$$(1 - \phi) \frac{d}{d\phi} [K^*(\phi)] = (K_i - K^*(\phi)) P^*(\phi), \quad (1)$$

$$(1 - \phi) \frac{d}{d\phi} [G^*(\phi)] = (G_i - G^*(\phi)) Q^*(\phi), \quad (2)$$

165 with initial conditions $K^*(0) = K_0$ and $G^*(0) = G_0$, where K_0 and G_0 are the bulk and
 166 shear moduli of the porosity-free material, respectively; K_i and G_i are the bulk and shear
 167 moduli of the pore-filling phase, respectively; and ϕ is the porosity. P^* and Q^* are the
 168 volumetric and deviatoric strain concentration factors for a penny-shaped pores (cracks),
 169 respectively, described as follows:

$$P^* = \frac{K^* + \frac{4}{3}G_i}{K_i + \frac{4}{3}G_i + \pi\alpha\beta^*}, \quad (3)$$

$$Q^* = \frac{1}{5} \left[1 + \frac{8G^*}{4G_i + \pi\alpha(G^* + 2\beta^*)} + \frac{2K_i + \frac{4}{3}(G_i + G^*)}{K_i + \frac{4}{3}G_i + \pi\alpha\beta^*} \right], \quad (4)$$

$$\beta^* = G^* \frac{3K^* + G^*}{3K^* + 4G^*}, \quad (5)$$

170 where α is the mean aspect ratio of cracks (defined as $\alpha = w/c$), with c and w being the
 171 mean pore radius and aperture, respectively. These equations indicate that the effective
 172 elastic wave velocity under wet conditions can be predicted from its dry velocity if the
 173 relationships among elastic wave velocity, porosity, and aspect ratio for the Susaki cores
 174 are known.

175 Here, we use the relationships among elastic wave velocity, porosity, and aspect ratio for
 176 the Susaki cores that were obtained by Okuda et al. (2024), who measured the P- and
 177 S-wave velocities and porosity of discrete cylindrical samples taken from the core. Those
 178 authors found that the porosity of the core ranged from 1% to 4% and that the relation-
 179 ship between velocity and porosity generally fell between the trends for $\alpha = 0.01$ and
 180 $\alpha = 0.03$. We therefore assumed an average aspect ratio of 0.02 for modeling the wet ve-
 181 locities and porosity from the dry velocities that we measured. The porosity-free elastic
 182 moduli were taken to be $K_0 = 64$ GPa and $G_0 = 37$ GPa, which were estimated from the
 183 velocity–porosity relationship established for the Susaki cores (Okuda et al., 2024). The
 184 bulk modulus for the inclusion phase was set as 0 GPa for dry air and 2.2 GPa for water,
 185 whereas the shear modulus was 0 GPa for both conditions.

186 Effective medium models postulate non-isobaric conditions for pore fluid within any unit
 187 volume (i.e., representative elementary volume: REV) and are applicable to the high-
 188 frequency regime without equilibration of pore pressure (i.e., pore pressure differs from
 189 crack to crack) during loading. Here, the logging measurements were performed at a fre-
 190 quency of ~ 15 kHz, which can lie within the validity range of effective medium models
 191 (Fortin & Guéguen, 2021).

192 4 Results and discussion

193 4.1 Ultrasonic velocity profiles

194 Ultrasonic P-wave velocity profiles for each analyzed depth interval of the studied core
195 are shown in Figure 4a, c, and e. The velocity ranges broadly from 4 to 6 km/s, with a
196 median of 5.44 km/s for all three layers. The sandstone layer has slightly higher veloc-
197 ity (median of 5.55 km/s) than the mudstone layers (median of 5.38 km/s). These re-
198 sults are consistent with laboratory results using discrete cylindrical samples taken from
199 the Susaki cores (Okuda et al., 2024), are similar to high-velocity zones observed at the
200 Nankai Trough (Kamei et al., 2013; Shiraishi et al., 2019), and are higher than those mea-
201 sured on other core samples from the Nankai subduction zone and the Shimanto accre-
202 tionary complex (Hamahashi et al., 2013; Tsuji et al., 2006).

203 Figure 4b, d, and f shows microscale porosity profiles estimated via the DEM model, as-
204 suming a mean crack aspect ratio of 0.02. The porosity ranges from 0.5% to 4%, with a
205 median of 1.3%. The sandstone layer has slightly lower porosity (median of 1.1%) than
206 the mudstone layers (median of 1.4%). Given the ultrasonic wavelength used here of 4–6
207 mm, these porosity variations indicate a heterogeneous distribution of millimeter to sub-
208 millimeter scale defects. Microstructural observations of these core samples indicated that
209 pressure solution processes, possibly driven by fluid migration, can have lowered the mi-
210 crocrack density and that variations in microscopic porosity are due mainly to variation
211 in pore space along clay minerals, such as illite and chlorite (Okuda et al., 2024). Miner-
212 alogical analyses have also indicated that the mudstone samples have high clay mineral
213 contents compared with the sandstones (Okuda et al., 2024), which is consistent with the
214 relatively high porosity of the mudstone layers measured in this study. These observations
215 suggest that the spatial variations in microscopic porosity can be attributed partly to clay
216 mineral contents. Nevertheless, there are localized high-porosity zones, particularly in the
217 sandstone layer (Figure 4d), which may be attributable to localized areas of intense brittle
218 damage.

219 To compare the ultrasonic velocity profiles measured under dry conditions with sonic log-
220 ging velocity measured under water-saturated conditions, we modeled ultrasonic velocity
221 under wet conditions from the dry velocity and porosity via DEM. The modeled veloci-
222 ties are higher than the dry velocities, ranging from 5.0 to 6.1 km/s (Figure 5). Compared
223 with the sonic logging velocities, these velocities are also higher by 0.1–2.1 km/s. This
224 means that the observed sonic velocities cannot be explained by water-saturated micro-
225 scopic porosity alone. Given that natural geological systems contain defects of different
226 scales, the decrease in P-wave velocity of the Susaki core from ultrasonic to sonic scales
227 implies the additional contribution of relatively large-scale porosities that are invisible via
228 ultrasonic velocities.

229 4.2 Estimation of mesoscale porosity

230 To account for the discrepancies between the sonic and ultrasonic velocities, we in-
231 troduced an effective medium model that includes mesoscale porosity in addition to
232 microscale porosity, on the basis of DEM theory (Figure 6). As described in the previous
233 section, the effective elastic properties estimated via ultrasonic velocity can be expressed
234 as a matrix phase containing (randomly oriented) penny-shaped cracks of a given mean

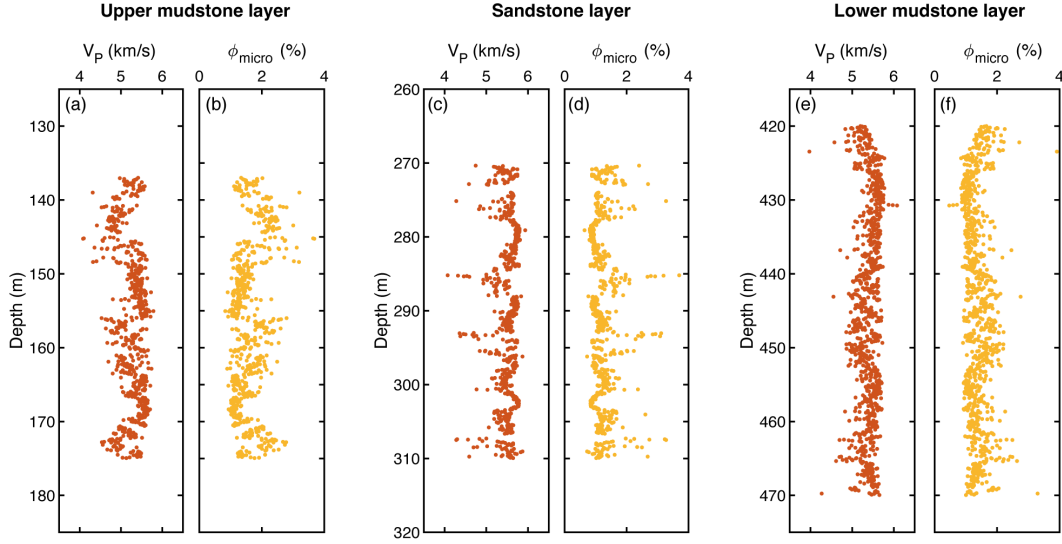


Figure 4 Depth variations in ultrasonic P-wave velocity (a, c, and e) and microscale porosity estimated from the DEM model (b, d, and f) for each analyzed depth interval of the studies core.

235 aspect ratio (Equations 1, 2, 3, 4, 5). At the sonic wavelength scale (mesoscale), such an
 236 effective medium including microscopic porosity should be regarded as a matrix phase,
 237 and the effective elastic properties can be expressed by introducing a second family of
 238 mesoscale inclusions that are larger than the ultrasonic wavelength but smaller than
 239 the sonic wavelength (Figure 6) (Bailey et al., 2019). Consequently, the effective elastic
 240 properties estimated via sonic velocity (K^{**} and G^{**}) can be expressed as follows:

$$(1 - \phi_{\text{meso}}) \frac{d}{d\phi_{\text{meso}}} [K^{**}(\phi_{\text{meso}})] = (K_i - K^{**}(\phi_{\text{meso}})) P^{**}(\phi_{\text{meso}}), \quad (6)$$

$$(1 - \phi_{\text{meso}}) \frac{d}{d\phi_{\text{meso}}} [G^{**}(\phi_{\text{meso}})] = (G_i - G^{**}(\phi_{\text{meso}})) Q^{**}(\phi_{\text{meso}}), \quad (7)$$

241 with the initial conditions $K^{**}(0) = K^*(\phi_{\text{micro}})$ and $G^{**}(0) = G^*(\phi_{\text{micro}})$, where ϕ_{micro}
 242 and ϕ_{meso} are the microscale and mesoscale porosities, respectively, and the total porosity
 243 is $\phi_{\text{total}} = \phi_{\text{micro}} + \phi_{\text{meso}}$. Here, we used P^{**} and Q^{**} for penny-shaped cracks assuming
 244 the mean aspect ratio of the mesoscale cracks to be 0.002. This value is based on a typi-
 245 cal value for vein minerals that are traces of mesoscale fractures (van Everdingen, 1995).
 246 Using this model and the microscale porosity determined in the previous section, we per-
 247 formed an inversion of the observed sonic velocity and estimated mesoscale porosity. The
 248 microscale porosity used at each depth was a moving average of 0.5 m based on the sonic
 249 wavelength (Figure 5).

250 Figure 7 shows the mesoscale porosity determined by the inversion of the sonic logging
 251 velocities, assuming a mean aspect ratio of mesoscale cracks of 0.002. The addition of

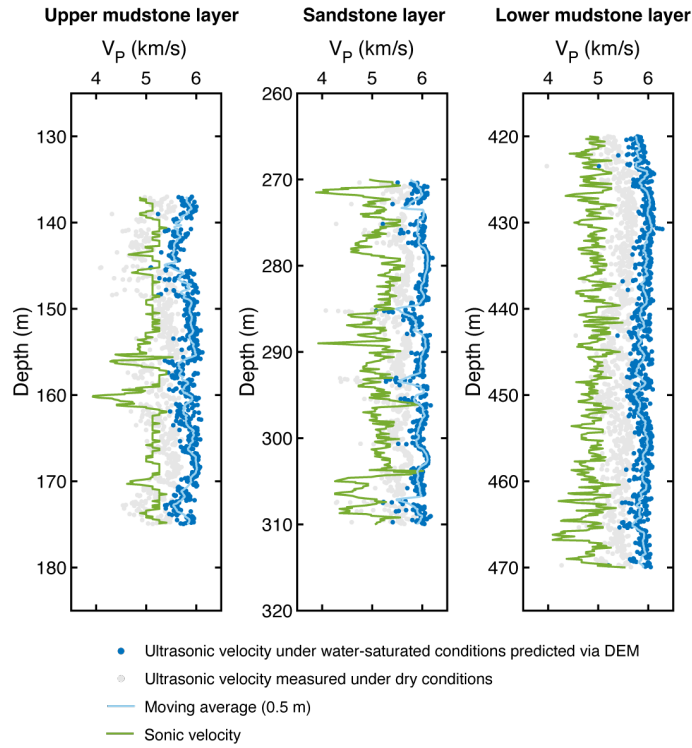


Figure 5 Comparison of modeled P-wave velocity under water-saturated conditions (blue dots) with that predicted from dry velocity (gray dots) via DEM, with sonic logging velocities (green lines) for each analyzed depth interval of the studied core.

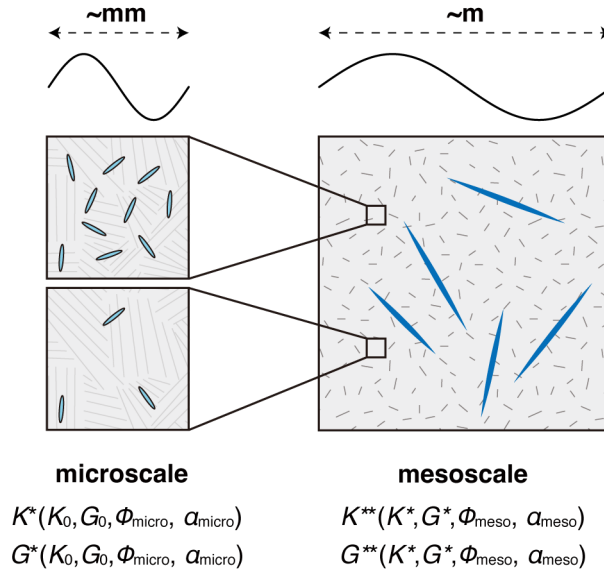


Figure 6 Schematic illustrations showing modeling of effective elastic properties at the micro- and mesoscales by adding water-saturated microcracks and mesoscale fractures observed by different wavelengths (frequencies).

252 mesoscale porosity of 0.1%–1.0% well explains the observed discrepancies between the
 253 ultrasonic and sonic velocities (Fig. S1). In contrast to the microscale porosity, the
 254 mesoscale porosity shows no clear difference between the sandstone layer (median of 0.5%)
 255 and the mudstone layers (median of 0.6%), implying that mesoscale fractures can develop
 256 regardless of lithology. According to the DEM model, mesoscale porosity with a low
 257 mean aspect ratio can readily decrease the elastic wave velocity compared with microscale
 258 porosity with a relatively high mean aspect ratio (Figure 9a).

259 As described in the previous section, the DEM model is considered valid primarily for
 260 a relatively high-frequency regime ($\leq\text{kHz}$) where non-isobaric pore pressure conditions
 261 within the homogeneous unit volume (REV) can be assumed (e.g., Mavko et al., 2020).
 262 Thus, care should be taken when modeling the effect of porosity at seismic frequencies
 263 ($\ll\text{kHz}$). However, our dense data indicate that the spatial distributions of ultrasonic-
 264 scale (4–6 mm) and sonic-scale (0.3–0.4 m) porosities are not homogeneous at scales larger
 265 than their wavelengths, implying that a larger REV of porosity at each scale can be valid
 266 for the seismic frequencies in the order of a Hz ($\sim\text{km}$). This could prolong the time for the
 267 pore pressure equilibration within a given REV and extend the applicability of the effective
 268 medium model to even lower frequencies (Akamatsu et al., 2024).

269 Our model also assumes an isotropic orientation of fractures. Nevertheless, actual
 270 mesoscale fractures may exhibit anisotropy if they were formed under a deviatoric stress
 271 field. Although it is difficult to constrain the influence of anisotropy on the sonic velocity
 272 from our dataset alone, the presence of mesoscale fractures remains necessary even if the
 273 effect of anisotropy is ignored.

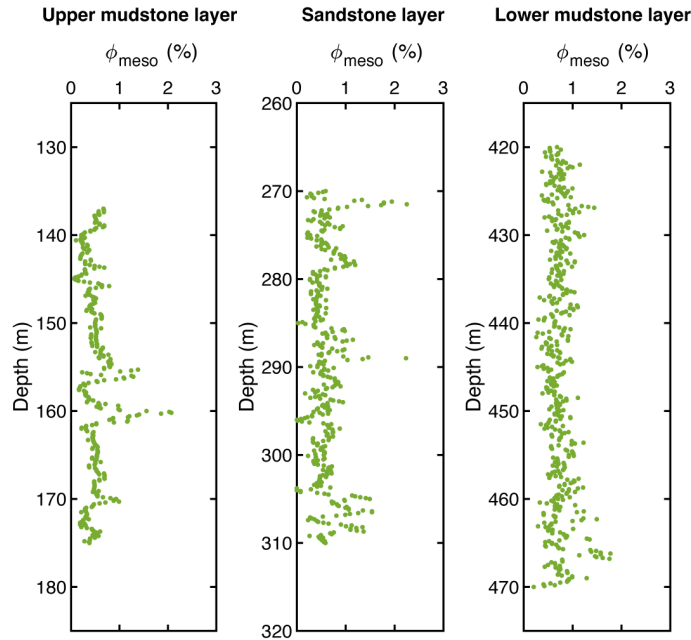


Figure 7 Mesoscale porosity estimated for each analyzed depth interval of the studied core.

274 4.3 Role of mesoscale fractures in subduction zones

275 Numerous seismological surveys have been conducted in subduction zones to explore the
 276 relationship between seismic activity and geophysical structure. In the Nankai Trough,
 277 seismic velocity structure has been acquired by seismic reflection surveys and waveform in-
 278 version techniques, and low- and high-velocity anomalies have been identified in the hang-
 279 ing wall side of the plate boundary fault (Kamei et al., 2013; Shiraishi et al., 2019). Given
 280 the in situ lithostatic pressure, the identified low-velocity anomalies have been interpreted
 281 as an indicator of extremely high pore-fluid pressure close to the lithostatic pressure (i.e.,
 282 low effective pressure) that can maintain open pore spaces (Kitajima & Saffer, 2012; Tsuji
 283 et al., 2014). This interpretation of velocity anomalies has been attributed to microscale
 284 pore space only because it is based on the velocity–porosity relationship for subduction-
 285 zone rocks established at ultrasonic frequency, i.e., microscale pore space (Hoffman &
 286 Tobin, 2004; Tsuji et al., 2006). However, our results demonstrate that the P-wave veloc-
 287 ity of subduction-zone rocks can readily decrease down to 5 km/s or even lower when a
 288 part of the total porosity is accommodated by the mesoscale fractures (Figure 9a). As the
 289 Susaki core without mesoscale fractures (i.e., measurements at the ultrasonic frequency)
 290 shows high velocities similar to those of high-velocity zones along the Nankai Trough, the
 291 variations in the seismic velocity observed in the Nankai Trough may reflect the distribu-
 292 tion of mesoscale fractures with high pore pressure.

293 It is to be noted that our estimates of mesoscale porosities for the Susaki cores could be
 294 formed during their exhumation processes. Thus, the mesoscale fractures estimated from
 295 the sonic logging at the Susaki boreholes are not the ones which are in deep subduction

296 zones. In fact, fluid-saturated fractures that were present at subduction plate interfaces
 297 can now be observed as veins (Muñoz-Montecinos & Behr, 2023; Otsubo et al., 2020; Ujiie
 298 et al., 2018). The Susaki cores commonly contain quartz veins with apertures of several
 299 tens to hundreds of microns (Figure 8). Such veins are possibly remnants of mesoscale
 300 fractures under high pore fluid pressure in the deep subduction zone before exhumation
 301 and likely affected seismic velocities in the subduction zones.

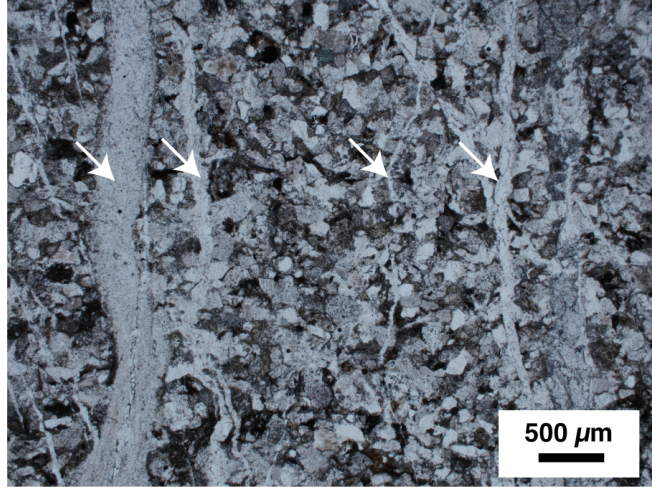


Figure 8 Representative photomicrographs (plane-polarized light) of sandstone from the Susaki core showing quartz veins (white arrows) with apertures of several tens to hundreds of microns.

302 Fluid migration through pore spaces may trigger characteristic seismic activity in subduc-
 303 tion zones (e.g., Tonegawa et al., 2022). The mesoscale fractures can act as effective fluid
 304 pathways and facilitate rapid fluid drainage in the deep subduction zone, since permeabil-
 305 ity of rock is also scale-dependent (Heap & Kennedy, 2016). The effective permeability of
 306 rock containing randomly oriented penny-shaped cracks k is given as follows:

$$k = \frac{2}{15} f \phi w^2, \quad (8)$$

307 where f is the connectivity of pore space ($0 \leq f \leq 1$), ϕ is the porosity, and w is the mean
 308 aperture of cracks (Guéguen & Palciauskas, 1994). This equation predicts the permeabil-
 309 ity to be strongly dependent on crack aperture. For a rock mass containing micro- and
 310 mesoscale porosities, the effective permeability can be expressed as follows:

$$k = k_{\text{micro}} + k_{\text{meso}} = \frac{2}{15} (f_{\text{micro}} \phi_{\text{micro}} w_{\text{micro}}^2 + f_{\text{meso}} \phi_{\text{meso}} w_{\text{meso}}^2), \quad (9)$$

311 where the subscripts denote each scale. Here, we incorporated this model into our up-
 312 scaled DEM model and estimated the relationship between V_p and k for subduction zones,
 313 which accounts for the scaling effect. First, we calculated V_p and k for microscale porosity

314 until V_P reaches the median of ultrasonic velocity of the Susaki core with a mean aspect
 315 ratio of 0.02. w_{micro} was set as 1 μm , based on microstructural observations (Okuda et al.,
 316 2024). We then added mesoscale porosity into the matrix phase with the microscale V_P
 317 and k until V_P reaches the median of sonic velocity of the Susaki area with a mean aspect
 318 ratio of 0.002. w_{meso} was set as 100 μm , based on the sonic wavelength and the assumed
 319 aspect ratio. Since the connectivity of pore space is not measurable from our data, we as-
 320 sumed $f = 1$ for each scale, and the estimated permeability should therefore be considered
 321 as the maximum value.

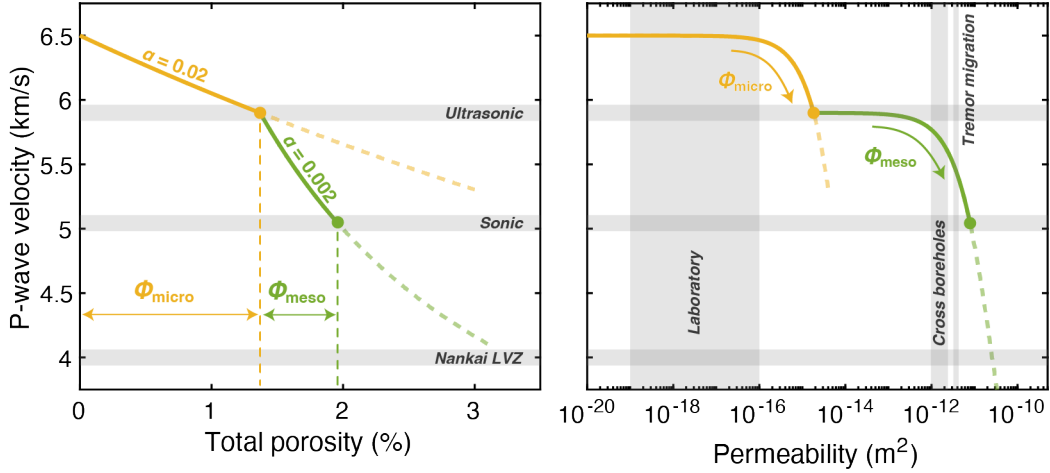


Figure 9 (a) P-wave velocity as a function of total porosity modeled for the median values of ultrasonic and sonic velocities obtained in this study (gray lines). Data from a low-velocity zone (LVZ) in the Nankai Trough (Shiraishi et al., 2019) is also presented. (b) Relationship between P-wave velocity and permeability modeled by incorporating micro- and mesoscale porosities. The vertical gray shadings represent values obtained from laboratory measurements using drill core samples from the Nankai Trough (Song & Underwood, 2017; Takahashi et al., 2013; Valdez et al., 2015), a cross-hole experiment in the Nankai Trough (Kinoshita & Saffer, 2018), and constraints based on tremor migration patterns observed in the Nankai Trough (Hendriyana & Tsuji, 2021).

322 Figure 9b shows the relationship between V_P and k modeled using the upscaled DEM
 323 model. The permeability initially increases by several orders of magnitude with decreasing
 324 velocity. As ϕ_{micro} increases, k increases up to 10^{-15} to 10^{-14} m^2 with a slight decrease
 325 in V_P , but the the rate of increase in permeability becomes more gradual once ϕ_{micro} no
 326 longer changes by orders of magnitude. Although these permeability values are 1–2 or-
 327 ders of magnitude higher than those typically measured for hand-sized sedimentary rocks
 328 in the laboratory (Song & Underwood, 2017; Takahashi et al., 2013; Valdez et al., 2015),
 329 this is likely resulted from a fixed crack aperture and assumption of perfectly connected
 330 pore spaces. When the effects of mesoscale porosity are included, k further increases by
 331 several orders of magnitude as V_P continues to decrease. Eventually, k increases to the or-
 332 der of 10^{-12} to 10^{-11} m^2 as V_P decreases to those of the sonic velocity in the Susaki area
 333 and a low-velocity zone in the Nankai Trough (Shiraishi et al., 2019). These permeability
 334 values cover the range of permeability determined at a scale of ~ 100 m by a cross-hole ex-
 335 periment in the Nankai Trough (Kinoshita & Saffer, 2018). Such high permeability values

336 are also required to explain tremor migration patterns observed in the Nankai subduc-
337 tion zone, which may represent fracture permeability that was enhanced during slow slip
338 events (Hendriyana & Tsuji, 2021). Our results suggest that mesoscale fractures consti-
339 tute highly permeable and low-velocity regions where characteristic seismic activity occurs
340 in subduction zones. In fact, temporal changes in seismic velocity structure observed in
341 the Nankai subduction zone have been shown to be associated with fluid migration before
342 slow earthquakes (Tonegawa et al., 2022).

343 5 Conclusions

344 To explore the scale dependence of seismic velocity in subduction zones, we compared ul-
345 trasonic and sonic velocities of core samples from the Susaki area in the Cretaceous Shi-
346 manto accretionary complex. The comparison revealed a decrease in P-wave velocity from
347 ~ 6 to 5 km/s with increasing scale, which we explain by accounting for mesoscale porosity.
348 This finding indicates that low-velocity anomalies observed along the Nankai Trough may
349 be associated with the presence of mesoscale fractures with high pore pressure. Mesoscale
350 fractures can also lead to high permeability in subduction zones of up to 10^{-12} to 10^{-11}
351 m^2 and hence effective fluid drainage. Seismic activity related to transient fluid migra-
352 tion around low-velocity zones could therefore be associated with the occurrence of the
353 mesoscale fractures.

354 Acknowledgements

355 We thank Satoshi Itaba (GSJ) for allowing the use of core samples and Tsutomu Kiguchi
356 (GSJ) for providing detailed information on borehole logging measurements. We are grate-
357 ful to Takahiro Suzuki (MWJ), Osamu Tadai (MWJ), and Rina Fukuchi (Naruto Educa-
358 tion Univ.) for supporting the laboratory measurements. This study was supported by
359 JSPS KAKENHI grants JP24H01039 (Grant-in-Aid for Transformative Research Areas
360 (A) “Science of Slow-to-Fast Earthquakes”) for Y. Akamatsu, JP23K19081 (Grant-in-Aid
361 for Research Activity Start-up) and JP24H01036 (Grant-in-Aid for Transformative Re-
362 search Areas (A) “Science of Slow-to-Fast Earthquakes”) for H. Okuda, and JP22K14112
363 (Grant-in-Aid for Early-Career Scientists) for M. Sawai.

364 Data availability statement

365 All the laboratory data and borehole logging data used in this study are provided in the
366 Supporting Information Tables S1 and S2.

367 References

368 Akamatsu, Y., Nagase, K., Abe, N., Okazaki, K., Hatakeyama, K., & Katayama, I. (2023).
369 Cross-property relationship between electrical resistivity and elastic wave velocity of
370 crustal rocks from the oman drilling project hole GT3A: Implications for in situ geo-
371 physical properties of oceanic crust. *Journal of Geophysical Research, [Solid Earth]*,
372 *128*. <https://doi.org/10.1029/2022jb026130>

- 373 Akamatsu, Y., Kuwatani, T., & Katayama, I. (2024). Spatial heterogeneity of pore struc-
374 ture in the crustal section of the samail ophiolite: Implications for high VP/VS anoma-
375 lies in subducting oceanic crust. *Geophysical Research Letters*, *51*, e2023GL106943.
376 <https://doi.org/10.1029/2023GL106943>
- 377 Audet, P., & Schwartz, S. Y. (2013). Hydrologic control of forearc strength and seismicity
378 in the costa rican subduction zone. *Nature Geoscience*, *6*, 852–855. <https://doi.org/10.1038/ngeo1927>
- 380 Bailly, C., Fortin, J., Adelinet, M., & Hamon, Y. (2019). Upscaling of elastic properties in
381 carbonates: A modeling approach based on a multiscale geophysical data set. *Journal*
382 *of Geophysical Research, [Solid Earth]*, *124*, 13021–13038. [https://doi.org/10.1029/](https://doi.org/10.1029/2019jb018391)
383 [2019jb018391](https://doi.org/10.1029/2019jb018391)
- 384 Berryman, J. G., Pride, S. R., & Wang, H. F. (2002). A differential scheme for elastic
385 properties of rocks with dry or saturated cracks. *Geophysical Journal International*,
386 *151*, 597–611. <https://doi.org/10.1046/j.1365-246X.2002.01801.x>
- 387 Eberhart-Phillips, D., Bannister, S., & Reyners, M. (2017). Deciphering the 3-D distribu-
388 tion of fluid along the shallow hikurangi subduction zone using P- and S-wave attenua-
389 tion. *Geophysical Journal International*, *211*, 1032–1045. [https://doi.org/10.1093/gji/](https://doi.org/10.1093/gji/ggx348)
390 [ggx348](https://doi.org/10.1093/gji/ggx348)
- 391 Fortin, J., & Guéguen, Y. (2021). Porous and cracked rocks elasticity: Macroscopic poroe-
392 lasticity and effective media theory. *Mathematics and Mechanics of Solids: MMS*, *26*,
393 1158–1172. <https://doi.org/10.1177/10812865211022034>
- 394 Guéguen, Y., & Palciauskas, V. (1994). *Introduction to the physics of rocks*. Princeton
395 University Press.
- 396 Hamahashi, M., Saito, S., Kimura, G., Yamaguchi, A., Fukuchi, R., Kameda, J., et al.
397 (2013). Contrasts in physical properties between the hanging wall and footwall of
398 an exhumed seismogenic megasplay fault in a subduction zone—an example from the
399 nobeoka thrust drilling project. *Geochemistry, Geophysics, Geosystems*, *14*, 5354–5370.
400 <https://doi.org/10.1002/2013gc004818>
- 401 Hashimoto, Y., Eida, M., Kirikawa, T., Iida, R., Takagi, M., Furuya, N., et al. (2012).
402 Large amount of fluid migration around shallow seismogenic depth preserved in tec-
403 tonic mélange: Yokonami mélange, the cretaceous shimanto belt, kochi, southwest
404 japan. *Island Arc*, *21*, 53–64. <https://doi.org/10.1111/j.1440-1738.2011.00806.x>
- 405 Heap, M. J., & Kennedy, B. M. (2016). Exploring the scale-dependent permeability of
406 fractured andesite. *Earth and Planetary Science Letters*, *447*, 139–150. [https://doi.](https://doi.org/10.1016/j.epsl.2016.05.004)
407 [org/10.1016/j.epsl.2016.05.004](https://doi.org/10.1016/j.epsl.2016.05.004)
- 408 Hendriyana, A., & Tsuji, T. (2021). Influence of structure and pore pressure of plate in-
409 terface on tectonic tremor in the nankai subduction zone, japan. *Earth and Planetary*
410 *Science Letters*, *558*, 116742. <https://doi.org/10.1016/j.epsl.2021.116742>
- 411 Hoffman, N. W., & Tobin, H. J. (2004). An empirical relationship between velocity and
412 porosity for underthrust sediments in the nankai trough accretionary prism. *Proc.*
413 *Ocean Drill. Program Sci. Results*, *190*, 196, 1–23.
- 414 Ide, S. (2010). Striations, duration, migration and tidal response in deep tremor. *Nature*,
415 *466*, 356–359. <https://doi.org/10.1038/nature09251>
- 416 Itaba, S., Umeda, Y., Koizumi, N., Watanabe, H., Nakayama, N., & Sakai, S. (2014). *Ge-*
417 *ological data of the GSJ boring core at the susaki-otani observation station* (research
418 report No. 595). Geol. Surv. Japan, AIST.
- 419 Kamei, R., Pratt, R. G., & Tsuji, T. (2013). On acoustic waveform tomography of wide-
420 angle OBS data—strategies for pre-conditioning and inversion. *Geophysical Journal*

- 421 *International*, 194, 1250–1280. <https://doi.org/10.1093/gji/ggt165>
- 422 Kinoshita, C., & Saffer, D. M. (2018). In situ permeability and scale dependence of an
423 active accretionary prism determined from cross-borehole experiments. *Geophysical*
424 *Research Letters*, 45, 6935–6943. <https://doi.org/10.1029/2018gl078304>
- 425 Kitajima, H., & Saffer, D. M. (2012). Elevated pore pressure and anomalously low stress
426 in regions of low frequency earthquakes along the nankai trough subduction megathrust.
427 *Geophysical Research Letters*. <https://doi.org/10.1029/2012GL053793>
- 428 Kitamura, M., Hirose, T., & Lei, X. (2021). Mechanical weakness of the nankai accre-
429 tionary prism: Insights from V_p measurements of drill cuttings. *Geochemistry, Geo-*
430 *physics, Geosystems*, 22. <https://doi.org/10.1029/2020gc009536>
- 431 Matonti, C., Guglielmi, Y., Viseur, S., Bruna, P. O., Borgomano, J., Dahl, C., & Marié, L.
432 (2015). Heterogeneities and diagenetic control on the spatial distribution of carbonate
433 rocks acoustic properties at the outcrop scale. *Tectonophysics*, 638, 94–111. <https://doi.org/10.1016/j.tecto.2014.10.020>
- 434 Mavko, G., Mukerji, T., & Dvorkin, J. (2020). *The rock physics handbook*. Cambridge
435 University Press.
- 436 Muñoz-Montecinos, J., & Behr, W. M. (2023). Transient permeability of a deep-seated
437 subduction interface shear zone. *Geophysical Research Letters*, 50. <https://doi.org/10.1029/2023gl104244>
- 438 Okuda, H., Akamatsu, Y., Kitamura, M., & Sawai, M. (2024). Elastic properties of hang-
439 ing wall rock at the seismogenic zone and critical nucleation length for megathrust
440 earthquakes. *ESS Open Archive*. <https://doi.org/10.22541/essoar.171838469.98902412/v1>
- 441
442
443
- 444 Otsubo, M., Hardebeck, J. L., Miyakawa, A., Yamaguchi, A., & Kimura, G. (2020). Lo-
445 calized fluid discharge by tensile cracking during the post-seismic period in subduction
446 zones. *Scientific Reports*, 10, 12281. <https://doi.org/10.1038/s41598-020-68418-z>
- 447 Raimbourg, H., Hamano, Y., Saito, S., et al. (2011). Acoustic and mechanical properties
448 of nankai accretionary prism core samples. *Geochemistry: Exploration, Environment,*
449 *Analysis*. <https://doi.org/10.1029/2010GC003169>
- 450 Saffer, D. (2003). Pore pressure development and progressive dewatering in underthrust
451 sediments at the costa rican subduction margin: Comparison with northern barba-
452 dos and nankai. *Journal of Geophysical Research*, 108, 2261. <https://doi.org/10.1029/2002JB001787>
- 453
- 454 Saffer, D. M., & Tobin, H. J. (2011). Hydrogeology and mechanics of subduction zone
455 forearcs: Fluid flow and pore pressure. *Annual Review of Earth and Planetary Sci-*
456 *ences*, 39, 157–186. <https://doi.org/10.1146/annurev-earth-040610-133408>
- 457 Sakaguchi, A. (1999). Thermal maturity in the shimanto accretionary prism, southwest
458 japan, with the thermal change of the subducting slab: Fluid inclusion and vitrinite
459 reflectance study. *Earth and Planetary Science Letters*, 173, 61–74. [https://doi.org/10.1016/S0012-821X\(99\)00219-8](https://doi.org/10.1016/S0012-821X(99)00219-8)
- 460
- 461 Sarout, J., Ferjani, M., & Guéguen, Y. (2009). A semi-automatic processing technique
462 for elastic-wave laboratory data. *Ultrasonics*, 49, 452–458. <https://doi.org/10.1016/j.ultras.2008.12.001>
- 463
- 464 Shiraishi, K., Moore, G. F., Yamada, Y., Kinoshita, M., Sanada, Y., & Kimura, G. (2019).
465 Seismogenic zone structures revealed by improved 3-D seismic images in the nankai
466 trough off kumano. *Geochemistry, Geophysics, Geosystems*. <https://doi.org/10.1029/2018gc008173>
- 467
- 468 Song, C., & Underwood, M. B. (2017). Data report: Permeability and microfabric of core

469 samples from IODP expedition 348, hole C0002P, nankai trough accretionary prism.
 470 In *Proceedings of the IODP*. Integrated Ocean Drilling Program. [https://doi.org/10.](https://doi.org/10.2204/iodp.proc.348.201.2017)
 471 [2204/iodp.proc.348.201.2017](https://doi.org/10.2204/iodp.proc.348.201.2017)
 472 Taira, A. (1988). The shimanto belt in shikoku, japan-evolution of cretaceous to miocene
 473 accretionary prism. *Shimanto Belt, Modern Geology*, *12*, 5–46.
 474 Takahashi, M., Azuma, S., Uehara, S.-I., Kanagawa, K., & Inoue, A. (2013). Contrasting
 475 hydrological and mechanical properties of clayey and silty muds cored from the shal-
 476 low nankai trough accretionary prism. *Tectonophysics*, *600*, 63–74. [https://doi.org/10.](https://doi.org/10.1016/j.tecto.2013.01.008)
 477 [1016/j.tecto.2013.01.008](https://doi.org/10.1016/j.tecto.2013.01.008)
 478 Tonegawa, T., Takemura, S., Yabe, S., & Yomogida, K. (2022). Fluid migration before
 479 and during slow earthquakes in the shallow nankai subduction zone. *Journal of Geo-*
 480 *physical Research*, [*Solid Earth*], *127*. <https://doi.org/10.1029/2021jb023583>
 481 Tsuji, T., Kimura, G., Okamoto, S., Kono, F., Mochinaga, H., Saeki, T., & Tokuyama, H.
 482 (2006). Modern and ancient seismogenic out-of-sequence thrusts in the nankai accre-
 483 tionary prism: Comparison of laboratory-derived physical properties and seismic reflec-
 484 tion data. *Geophysical Research Letters*, *33*. <https://doi.org/10.1029/2006GL027025>
 485 Tsuji, T., Kamei, R., & Pratt, R. G. (2014). Pore pressure distribution of a mega-splay
 486 fault system in the nankai trough subduction zone: Insight into up-dip extent of the
 487 seismogenic zone. *Earth and Planetary Science Letters*, *396*, 165–178. [https://doi.org/](https://doi.org/10.1016/j.epsl.2014.04.011)
 488 [10.1016/j.epsl.2014.04.011](https://doi.org/10.1016/j.epsl.2014.04.011)
 489 Ujiie, K., Saishu, H., Fagereng, Å., Nishiyama, N., Otsubo, M., Masuyama, H., & Kagi, H.
 490 (2018). An explanation of episodic tremor and slow slip constrained by crack-seal veins
 491 and viscous shear in subduction mélange. *Geophysical Research Letters*, *45*, 5371–5379.
 492 <https://doi.org/10.1029/2018gl078374>
 493 Valdez, R. D., II, Lauer, R. M., Ikari, M. J., Kitajima, H., & Saffer, D. M. (2015). Data
 494 report: Permeability and consolidation behavior of sediments from the northern japan
 495 trench subduction zone, IODP site C0019. In *Proceedings of the IODP*. Integrated
 496 Ocean Drilling Program. <https://doi.org/10.2204/iodp.proc.343343t.201.2015>
 497 van Everdingen. (1995). Fracture characteristics of the sheeted dike complex, troodos
 498 ophiolite, cyprus: Implications for permeability of oceanic crust. *Journal of Geophys-*
 499 *ical Research*, *100*, 19957–19972. <https://doi.org/10.1029/95JB01575>